Journal of Applied Polymer Science

Preparation of PVDF/$CaCO_3$ hybrid hollow fiber membranes for direct contact membrane distillation through TIPS method

Yang Song,[1,2,3,4,5] Ziyi Wang,[2,3,4,5] Qin Wang,[2,3,4,5] Baoan Li,[2,3,4,5] Benhe Zhong[1]

[1]College of Chemical Engineering, Sichuan University, Chengdu 610065, People's Republic of China
[2]State Key Laboratory of Chemical Engineering, Tianjin University, Tianjin 300072, People's Republic of China
[3]Chemical Engineering Research Center, School of Chemical Engineering and Technology, Tianjin University, Tianjin 300072, People's Republic of China
[4]Collaborative Innovation Center of Chemistry & Chemical Engineering (Tianjin), Tianjin 300072, People's Republic of China
[5]Tianjin Key Laboratory of Membrane Science and Desalination Technology, Tianjin University, Tianjin 300072, People's Republic of China
Correspondence to: B. Li (E-mail: libaoan@tju.edu.cn)

ABSTRACT: Poly(vinylidene fluoride) (PVDF)–$CaCO_3$ hybrid hollow fiber membranes with a cellular structure and prominent permeability were fabricated via the thermally induced phase separation method for membrane distillation. $CaCO_3$ nanoparticles were introduced to the casting solution to improve the properties of the membranes. The effect of $CaCO_3$ dosage on the morphology was investigated. The prepared membranes were characterized by differential scanning calorimetry, SEM, and atomic force microscopy. The results showed that liquid–liquid phase separation preceded solid–liquid phase separation during the spinning process. Low dosages of $CaCO_3$ had a strong influence on the crystallization of PVDF molecules. The contact angle of the membrane increased with the addition of $CaCO_3$ nanoparticles. The maximum dead end pure water flux was as high as 1295.5 L/(m^2 h). The direct-contact membrane distillation flux of the optimized PVDF/$CaCO_3$ hybrid membrane achieved 63.98 kg/(m^2 h) at the feed temperature of 90 °C. © 2016 Wiley Periodicals, Inc. J. Appl. Polym. Sci. **2016**, *133*, 43372.

KEYWORDS: fibers; membranes; porous materials; properties and characterization; separation techniques

Received 7 September 2015; accepted 19 December 2015
DOI: 10.1002/app.43372

INTRODUCTION

The membrane distillation (MD)[1,2] technique, a combination of membrane separation technology and traditional distillation technology, has been widely applied in chemical separation and enrichment, seawater desalination, and industrial wastewater treatment.[3–5] The membrane, which is employed as the physical barrier between two phases and provides a vapor-liquid interface for heat and mass exchanges, plays a very important role in the MD process.[6] Poly(vinylidene fluoride) (PVDF), with its excellent properties that include high mechanical strength, outstanding thermal stability, and resistance against corrosive chemicals, has been regarded as a preferred material for the MD technique.[7–9] There are mainly three methods, which are listed in Table I,[10–16] applied for preparing hollow fibers. It can be seen from Table I that the thermally induced phase separation (TIPS) method is the most suitable process to fabricate a membrane that has homogenous pore size distribution and high porosity.

In the TIPS process, a polymer is dissolved in a low-molecular-weight diluent with high boiling point at elevated temperature to form a homogeneous casting solution that is shaped into a flat or hollow fiber membrane after cooling in the coagulation bath to induce phase separation and solidify the membrane. In the final stage of the membrane fabrication, the residual diluent is extracted by another solvent, and then the solvent is removed to produce a microporous structure.[17,18]

Recently, a few articles reported that the addition of inorganic materials into a polymer solution in the preparation of PVDF membranes not only changed the porous structure, but also enhanced the properties of the membranes. The particles that were introduced into the membranes included TiO_2,[19–21] SiO_2,[22] ZnO,[23] Al_2O_3,[24,25] and ZrO.[26] Ngang *et al.* blended TiO_2 nanoparticles in a polymer solution via the non-solvent-induced phase separation (NIPS) process.[27] The test results showed that both the hydrophilicity and permeation flux of the modified PVDF membranes were greatly improved. Cui *et al.* prepared a PVDF/SiO_2 composite membrane that showed higher water flux and tensile strength

Table I. Characteristic of Methods Applied for Preparing Hollow Fibers

Method	Advantages	Disadvantages
Melt-spinning and cold-stretching (MSCS)	Less amount of solvents or diluents,[10] clean and economical process[11]	Difficult control of the membrane structure,[12] rigorous technology for pore formation
Non-solvent-induced phase separation (NIPS)	Mild conditions, simple fabrication process,[13] wide application[14]	Poor mechanical properties, wide pore size distribution, difficult recovery of solvent[14]
Thermally induced phase separation (TIPS)	Well-controlled procedure, narrow pore size distribution,[15] high porosity, better mechanical properties[16]	High energy consumption, difficult recovery of solvent

compared with that of the neat polymeric membrane.[28] A membrane designed for the MD process should be hydrophobic and only allow vapor molecules to pass through.[14,29] Therefore, the introduction of hydrophobic nanoparticles in the membrane fabrication process may be an effective method to improve the hydrophobicity and permeability of membranes for the MD process.

Nano-$CaCO_3$ is a kind of common and low-price addition that shows a favorable dispersity in organic diluent and high interface adhesive force with the polymer matrix.[30] Li *et al.* investigated the influence of $CaCO_3$ nanoparticles on the morphology and strength of a PVDF flat membrane prepared via the TIPS process.[31] The results showed that the spherulitic morphology of membranes had obviously changed with the different $CaCO_3$ dosages, while the existence of $CaCO_3$ had a negative effect on the mechanical strength of the membrane. However, Li did not explain the formation mechanism of the morphologies in the phase-separation process in detail, and further investigation on the membrane properties, such as porosity, pore size distribution, and water flux, was lacking. Hou *et al.* prepared PVDF/$CaCO_3$ hollow fiber membranes for MD through the NIPS method.[32] The addition of $CaCO_3$ nanoparticles improved the crystallinity degree of PVDF and the hydrophobicity of the membranes. However, the finger-like macrovoids inside the membranes may affect the stability in applications.

In this work, PVDF hollow fiber membranes with a cellular structure were prepared from a ternary system that included PVDF, γ-butyrolactone (solvent), and dioctyl phthalate (nonsolvent) via the TIPS approach in an environmentally friendly way. Nitrogen was introduced as a bore fluid, and the primary membranes were cooled down to room temperature in air, which reduced the amount of solvent in the process. A few $CaCO_3$ nanoparticles were added into the spinning system to improve the spinnability of the casting solution and enhance the performance of the membranes. The aim of this study is to investigate the effects of various $CaCO_3$ dosages on the morphology, hydrophobicity, pore size, and mechanical properties of the PVDF hollow fibers. The permeability of the membranes in direct-contact membrane distillation (DCMD) was evaluated.

EXPERIMENTAL

Materials

The PVDF ($M_w = 2.55 \times 10^5$, $M_w/M_n = 1.9$) used in the study was provided by Solvay Solexis (Solef 6008, Brussels, Belgium). γ-Butyrolactone (γ-BL), dioctyl phthalate (DOP), ethanol (99.7 wt %), and nano-calcium carbonate ($CaCO_3$) were analytical reagents (AR grade) and purchased from Guangfu Fine Chemical Research Institute (Tianjin, China). All chemicals used in this study were not further purified. The boiling points of γ-BL (bp 358.8 °C) and DOP (bp 384.93 °C) are much higher than PVDF (164 °C).

Preparation of Hollow Fiber Membranes

The hollow fiber membranes were prepared by the TIPS method. The extrusion apparatus is shown in Figure 1. Before the preparation of the membrane, the nano-$CaCO_3$ particles were dried at 100 °C for 2 h to remove the water that might exist. Then the raw materials, γ-BL, DOP, and a certain amount of $CaCO_3$, were mixed in a flask and soaked in an ultrasonic bath for 30 min to disperse the $CaCO_3$ nanoparticles in the solvent. The mixed solvent and PVDF were added into a stainless steel vessel. The slurry was heated to 180 °C and stirred for 2 h under a nitrogen atmosphere. After releasing the bubbles for 3 h, the homogeneous casting solution was fed into a spinneret at the nitrogen pressure of 0.25 MPa, and the extrusion rate was 20 ml/min. Fibers were extruded through the spinneret, the

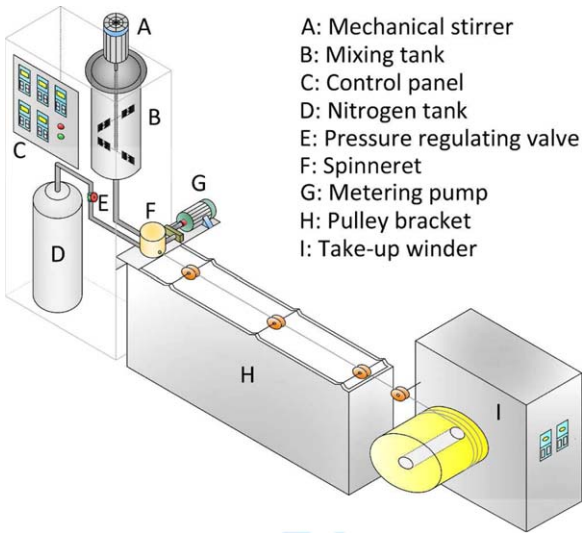

Figure 1. Schematic diagram of the preparation of the hollow fiber membranes by the TIPS method. [Color figure can be viewed in the online issue, which is available at wileyonlinelibrary.com.]

Table II. Some Parameters of the Membrane Fabrication Process

Sample	DOP/diluent mixture (wt %)	PVDF concentration (wt %)	$CaCO_3$/PVDF weight (wt %)	Outer diameter of fiber (μm)	Inner diameter of fiber (μm)
M-0	30	28	0	1156.62	746.98
M-1	30	28	1	1213.94	783.26
M-2	30	28	2	1091.76	653.12
M-3	30	28	3	1085.26	661.04
M-5	30	28	5	1239.88	829.36
M-8	30	28	8	1120.92	690.94

outer and inner diameters of which were 5.1 mm and 3.6 mm, respectively. Another stream of nitrogen was blown into the spinneret at a rate of 5 ml/min to make an open space at the center of the fiber. The nitrogen was heated to 100 °C by a heating jacket before entering the spinneret. The molten hollow fiber was cooled in air at the room temperature of 25 °C. The solidified hollow fiber membranes were rolled by a take-up machine with the rolling velocity of 5 m/min and further extracted by immersion in ethanol for 24 h to remove the residual solvent. The final membranes were dried in air at room temperature. The detailed parameters of the membrane fabrication process are listed in Table II.

Determination of the Phase Diagram

The crystallization temperature (T_C) of the membrane was measured by differential scanning calorimetry (DSC) (Perkin-Elmer, DSC-7, Waltham, Massachusetts).[33] A sample of about 5 mg of the membrane was sealed in an aluminum DSC pan, kept at 200 °C for 10 min to ensure a complete melt, and then cooled to 40 °C at a rate of 10 °C/min. The onset temperature of the exothermic peak during the cooling was taken as the T_C. The crystallinity degree X_c was evaluated by

$$X_c = \Delta H_c / \Delta H_f \times 100\% \quad (1)$$

The crystallization heat ΔH_c is determined from the exothermic peak area analyzed by Origin 9.0 software. The ΔH_f is the enthalpy for a 100% crystalline sample of PVDF, which is reported to be 104.7 J/g.[34]

The cloud points were used to describe the miscibility of the quaternary system. The sample was chopped into small pieces and placed in the hollow center of a microscope slide, and then sealed by another slide. A Teflon film with a square opening in the center was inserted between the slides to prevent diluent evaporation. The sample was heated on a hot stage to 200 °C for 10 min and cooled to room temperature at a controlled rate of 5 °C/min. The cloud-point temperature (T_{cloud}) was determined by an optical microscope (X-4D, Olympus (China) OC, Ltd, Beijing, China) when turbidity was observed.

Morphological Study of Hollow Fiber Membranes

The dry hollow fiber membranes were freeze-fractured in liquid nitrogen and treated with Au sputtering (Hitachi, E1020, Tokyo, Japan). The cross sections and the surfaces of the membranes were observed by a field-emitting scanning electron microscope (SEM) (Hitachi, S-4800).

The outer surface roughness of the membrane was studied with an atomic force microscope (AFM, AJ-IIIa, Shanghai AJ Development Company of Nano Science and Technology, Shanghai, China). All of the samples were measured by using the same tip with a scan area of 10.0 μm × 10.0 μm. The tapping mode was operated to obtain the membrane surface roughness. The average roughness was used to evaluate the morphology of the membrane.

Contact Angle Measurement of Hollow Fiber Membranes

Water contact angles were measured at 25 °C by the sessile drop method using a contact angle instrument (Dataphysics OCA15EC, Stuttgart, Germany). A length of dry fiber was split through the cross section and then fixed between two glass slides for 24 h to make the membrane surface flat. The volume of the deionized water droplet used in the measurement was 1 μl. Five different positions on the membrane surface were measured for the average contact angle value.

Porosity and Pore Size Distribution of Hollow Fiber Membranes

The overall porosity was determined by the gravimetric method. The dry membranes were immersed in ethanol for 24 h and taken out to be weighed immediately after removing ethanol from the surface. The porosity of the hollow fiber was calculated by the following equation[35]:

$$\varepsilon = \frac{(m_2 - m_1)\rho_1}{\rho_1 m_2 + (\rho_2 - \rho_1) m_1} \times 100\% \quad (2)$$

where m_1 is the weight of dry membrane, m_2 is the weight of wet membrane, ρ_1 is the density of the PVDF, and ρ_2 is the density of the wetting solution.

The apparatus for measuring the pore size distribution of the hollow fiber membranes is shown in Figure 2. Ethanol was added into the buffer tank. The Hagen–Poiseuille equation was used to obtain the pore size distribution of the hollow fiber:

$$J = \frac{\pi d_i^4}{128 \eta l} \Delta P_i \quad (3)$$

where J is the volumetric flow rate, d_i is the pore diameter, η is the coefficient of viscosity (dynamic), l is the length of a pore, and ΔP_i is the pressure difference.

Nitrogen was forced to permeate from the inside to the outside of the hollow fiber membranes. The pores were wetted by a

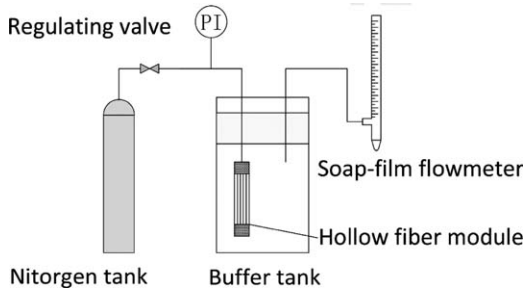

Figure 2. Apparatus for measuring the pore size distribution of the hollow fiber membranes.

99.7 wt % ethanol solution (surface tension 21.97 dym/cm) for 10 h previously. In the test process, the big pores with large diameters were burst first at a low nitrogen pressure. The smaller pores were opened gradually with the increase of nitrogen pressure. The smallest pores were penetrated finally at the highest pressure. The measured pore flow rate at ΔP_i was the cumulative overall pore flow rate J_i, which could be calculated from the distance that the bubble passed through the tube per second in the apparatus. According to eq. (3), the increase of overall pore area S_i was calculated as

$$S_i=\frac{\pi}{4}\left(D_i^2\text{-}D_{i\text{-}1}^2\right)=(8\pi\eta l)^{1/2}\left[\left(\frac{J_i}{\Delta P_i}\right)^{1/2}\text{-}\left(\frac{J_{i\text{-}1}}{\Delta P_{i\text{-}1}}\right)^{1/2}\right] \quad (4)$$

The pore diameter d_i was calculated according to the Laplace equation:

$$d_i=4\gamma\cos\theta/\Delta P_i \quad (5)$$

where γ is the surface tension of the wetting solution, and θ is the contact angle of the wetting solution. The pore number $N_{i-1,i}$ of the pore diameter from d_{i-1} to d_i was obtained as

$$N_{i\text{-}1,\ i}=\frac{S_i}{\frac{\pi}{4}\left(\frac{d_i+d_{i+1}}{2}\right)^2} \quad (6)$$

The pore size distribution was determined by

$$\text{Frequency}=\frac{N_{i\text{-}1,i}}{\sum_{i=1}^{m}N_{i\text{-}1,i}} \quad (7)$$

Mechanical Strength of Hollow Fiber Membranes

The tensile strength of the hollow fiber membranes was examined by a Universal Testing Machine (WD-10D, Changchun Second Material Testing Machine, Changchun, China). The effective length of each fiber was 100 mm. The membrane was extended at a constant elongation rate of 50 mm/min until it was broken. At least five fibers were tested, and the average data were taken for each sample.

Pure Water Flux of Hollow Fiber Membranes

The measuring device of pure water flux is shown in Figure 3. The test was performed with a dead-end-type membrane module that was sealed by epoxy resin. Because PVDF is a kind of hydrophobic material,[36] the module was immersed in ethanol for 24 h for prewetting before the test. The operating temperature was 25 °C. The air pressure was fixed at 0.1 MPa to provide a constant driving force for water to permeate from the inside to the outside of the hollow fiber membranes. The pure water flux of the membrane was evaluated on the basis of the inner surface area by the following equation:

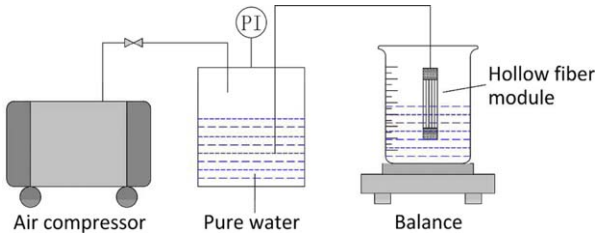

Figure 3. Apparatus for measuring pure water flux. [Color figure can be viewed in the online issue, which is available at wileyonlinelibrary.com.]

$$\text{Flux}\ \left(\text{L}/\left(\text{m}^2\text{atm h}\right)\right)=\frac{m_t}{2\pi\rho RL\Delta P_t t} \quad (8)$$

where m_t is the volume of water permeated through the membrane (L); ρ is the density of water used in the test; L is the measured fiber length (m); ΔP_t is the pressure difference in the test (atm); t is the test time (h); and R is the inside radius of the hollow fiber (m).

DCMD Flux of Hollow Fiber Membranes

The DCMD test was carried out to evaluate the permeability performance of the prepared hollow fiber membranes. Figure 4 shows the schematic diagram of the experimental apparatus for DCMD. Ten pieces of dry PVDF hollow fibers were assembled to be a submerged membrane module, and the two ends of the fiber bundle were sealed by epoxy resin. The effective length of the module was 200 mm. Five hollow fiber modules from the same spinning condition were fabricated for testing, and the average value was used for comparison. A hot NaCl solution (3.5 wt %), which was employed as the feed, was reserved in a thermostatic tank. Water was transferred across the membrane in the form of water vapor that flowed in the interior of the hollow fibers. The distilled water was cooled in the condenser and then flowed back to the distillate collector. The feed temperature was varied from 50 °C to 90 °C, and the cold distillate temperature was kept at 25 °C. The distillate flow rate was 0.80 m/s. The permeation quantity was measured and recorded by an online electrical balance. The salinity of the distillate was measured by a conductivity meter. The membrane distillation flux was calculated based on the inner surface area of the fibers by the following equation:

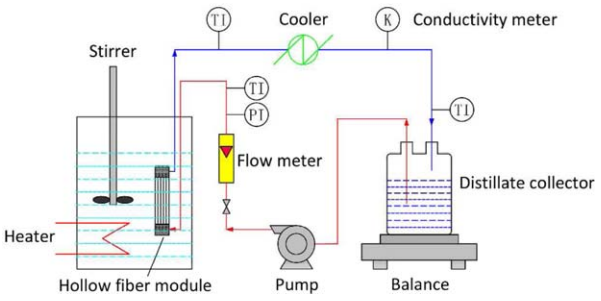

Figure 4. Apparatus for measuring membrane distillation flux. [Color figure can be viewed in the online issue, which is available at wileyonlinelibrary.com.]

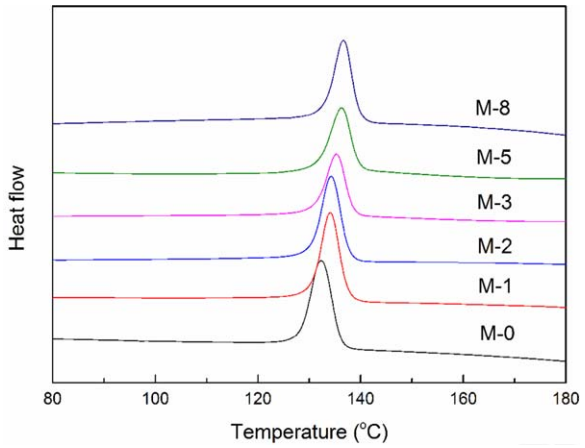

Figure 5. DSC curves of the membranes with different $CaCO_3$ dosages. [Color figure can be viewed in the online issue, which is available at wileyonlinelibrary.com.]

$$F = \frac{\Delta W}{A\Delta t} \quad (9)$$

where F is the permeate flux (kg/m^{2}h), ΔW is the weight of distillate (kg), A is the inner surface area of the hollow fiber membranes (m^2), and Δt is the testing time (h).

RESULTS AND DISCUSSION

DSC Analysis

The DSC curves of the PVDF membranes prepared with different $CaCO_3$ dosages are presented in Figure 5. It can be seen that the exothermic peaks migrated to the high-temperature region as the dosage of $CaCO_3$ increased. The shift of the exothermic peaks indicates that the addition of $CaCO_3$ nanoparticles improves the crystallization temperature (T_C) of the PVDF molecules. The data of ΔH_C and X_C are listed in Table III. With the increase of $CaCO_3$ dosage, the X_C of the hybrid membrane increases and reaches a maximum at the $CaCO_3$ dosage of 2 wt %. This proves that there were interactions between $CaCO_3$ nanoparticles and polymers. An appropriate dosage of $CaCO_3$ promotes the nucleation and accelerates the crystallization of PVDF molecules. However, the X_C begins to decrease from the M-3 hybrid membrane, which means that the redundant $CaCO_3$ nanoparticles are a disadvantage for the crystallization of the polymers. Similar results were obtained by Campos *et al.* in the preparation of a PVDF/$CaCO_3$ composite film.[37]

Table III. Crystallization Heat ΔH_C and Crystallinity Degree X_C of PVDF Membranes with Different $CaCO_3$ Dosages

Sample	ΔH_C (J/g)	X_C (%)
M-0	41.38	39.52
M-1	42.21	40.32
M-2	43.47	41.52
M-3	42.03	40.14
M-5	40.36	38.50
M-8	40.40	38.59

Phase Diagram

Phase separation in the TIPS process can be divided into two categories: solid–liquid (S-L) phase separation[38] and liquid–liquid (L-L) phase separation.[39] The order of phase separation determines the final morphology and structure of the membrane. The theoretical phase diagram in the TIPS process was reported in early years (shown as Figure 6).[12,40] The boundary line of the L-L phase separation region is usually named the binodal curve. The point on the binodal curve represents the cloud temperature (T_{cloud}) corresponding to a certain polymer concentration. Under the binodal curve, it is the spinodal curve that divides the L-L phase separation region into the metastable region and the unstable region. The L-L phase separation follows two different mechanisms, due to the existence of the binodal curve and the spinodal curve.[40] The relationship between the T_{cloud} curve and the crystallization curve was discussed in our previous report,[15,17] which provides a reference for the composition system in this work. Figure 6(a) shows a polymer/diluent system in which L-L phase separation occurs before S-L phase separation when the cooling route follows Approach 1. For a semicrystalline polymer, L-L phase separation leads to the formation of a polymer-rich phase and a polymer-lean phase. PVDF molecules migrate from the lean phase to the rich phase gradually as the temperature decreases. When the temperature arrives in the metastable region, a slight fluctuation in the system does not affect the stability of the system. When the system is quenched into the unstable region, all fluctuations in the system bring about a sharp decrease of free energy, and L-L phase separation takes place as a spinodal decomposition (SD) mechanism. When the temperature of the system continues to drop and reaches the crystallization curve, S-L phase separation occurs as a nucleation growth (NG) mechanism. Polymer crystallization is beneficial to the stabilization of the structure formed by L-L phase separation. A cellular structure is obtained through this phase separation approach.[41] Otherwise, S-L phase separation takes place ahead, shown as Approach 2 in Figure 6(b), resulting in a spherulitic structure.[12]

The phase diagram of the system in this work is shown in Figure 7. It can be seen from Figure 7 that the T_{cloud} curve is above the crystallization curve, which means that the L-L phase separation precedes the S-L phase separation as the temperature cools down in the system. The dosage of $CaCO_3$ has little effect on the T_{cloud}. However, the crystallization temperature rises slightly with the increase of $CaCO_3$ dosage. This is because

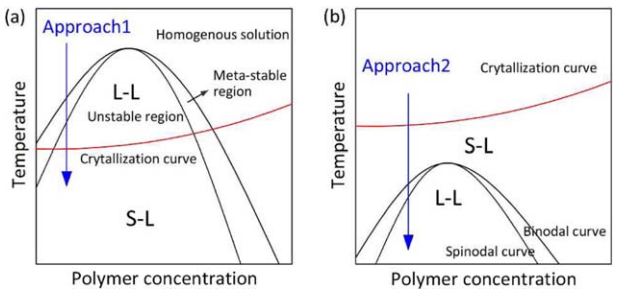

Figure 6. Theoretical phase diagrams in the TIPS process. [Color figure can be viewed in the online issue, which is available at wileyonlinelibrary.com.]

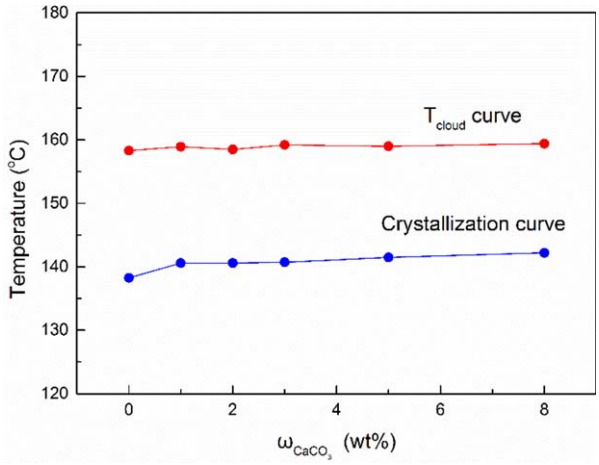

Figure 7. Phase diagram for the system in this work. [Color figure can be viewed in the online issue, which is available at wileyonlinelibrary.com.]

$CaCO_3$ nanoparticles provide many crystal nuclei in the system, which accelerates the PVDF crystallization process. It can be indicated that a desirable membrane cellular structure would be obtained.

Morphological Study of Membranes

The typical structures of the M-0 membrane are presented in Figure 8. As shown in Figure 8(b), the cross section of the M-0 membrane shows a cellular microstructure resulting from the suitable miscibility between PVDF and mixed diluent. It indicates that L-L phase separation occurred before crystallization, as discussed in the previous section.

Figure 8(c,d) shows the cross-sectional structures near the outer and inner surface. It can be seen that a thin skin layer emerged at the outer surface. In the process of membrane fabrication, the outer surface of the primary membrane was exposed to air. The evaporation of the diluent made the PVDF concentration increase accordingly. Thereby, the PVDF molecules tended to form a continuous phase at the outer surface. The temperature difference between air and the outer surface of the membrane was large enough, which made the crystallization of PVDF molecules very fast. The PVDF molecules connected to each other closely, which resulted in the formation of a dense skin. The pore size near the outer surface is smaller than that in the middle and near the inner surface in comparing Figure 8© with Figure 8(b,d). The space that was occupied by diluent became the pores after the diluent was extracted. The diluent concentration at the outer surface was lower than the other parts of the membrane because of diluent evaporation, which induced the smaller size of the pores.

Figure 8(e,f) shows the outer and inner surface structures. A dense skin at the outer surface is beneficial to the mechanical properties and the antipollution ability of the membrane. The outside and inside temperatures of the membrane were greatly different when the fiber was extruded from the spinneret. The inner surface cooled down from about 100 °C, which meant that S-L phase separation occurred in the cooling process (illustrated in Figure 7). There are many fuzzy microspheres in Figure 8(f) consequently. The cooling rate of the inner surface was slow enough for the fuzzy microspheres to impinge and connect to each other. Therefore, the gap pores among the microspheres emerged gradually.

The effect of $CaCO_3$ nanoparticles on the membrane structure is mainly embodied in the cross-sectional structure. The SEM images of the cross sections of membranes with different $CaCO_3$ dosages are shown in Figure 9. It can be seen from the figure that each sample has a cellular structure, while the penetrability and the number of the membrane pores have a slight

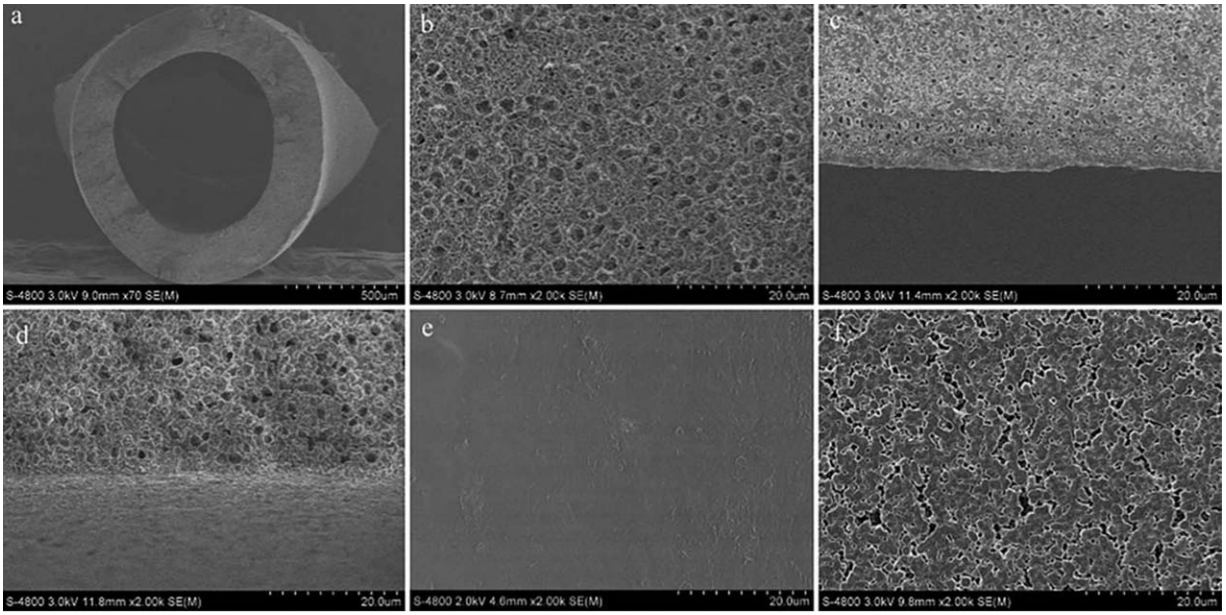

Figure 8. SEM morphologies of M-0: (a) panorama of the hollow fiber; (b) cross-sectional structure in the middle of the hollow fiber; (c) cross-sectional structure near the outer surface; (d) cross-sectional structure near the inner surface; (e) outer surface structure; (f) inner surface structure.

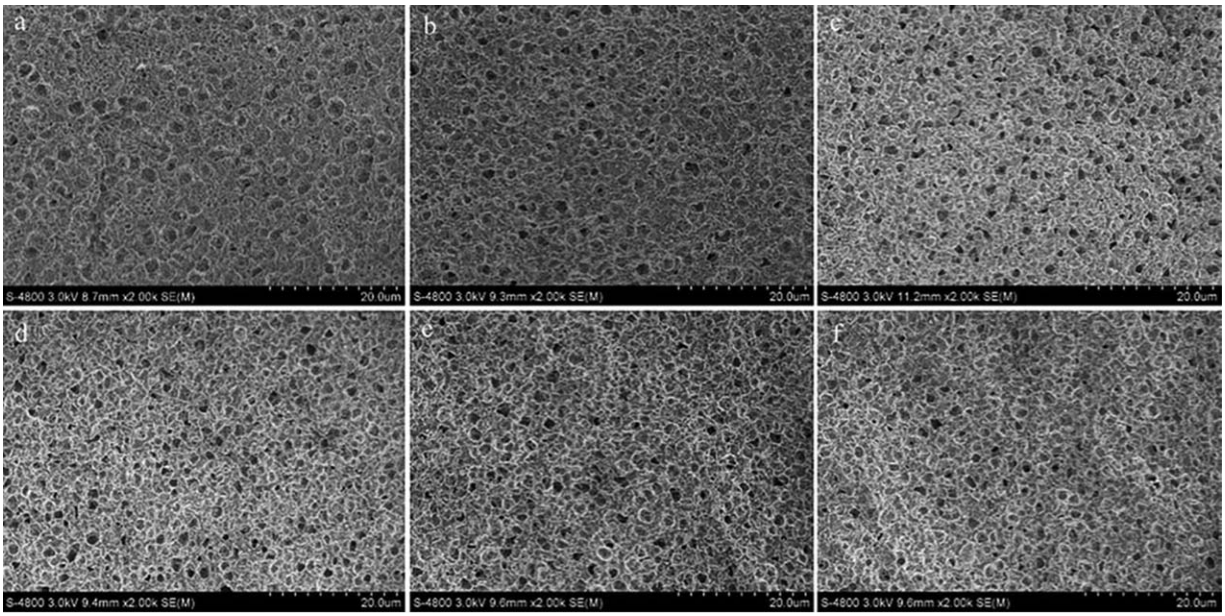

Figure 9. SEM images of the cross sections of membranes with different $CaCO_3$ dosages: (a) pure PVDF membrane; (b) 1% $CaCO_3$; (c) 2% $CaCO_3$; (d) 3% $CaCO_3$; (e) 5% $CaCO_3$; (f) 8% $CaCO_3$.

change. When the $CaCO_3$ dosage is no more than 2 wt %, the penetrability and the number of pores are improved with the increase in $CaCO_3$ dosage [shown as Figure 9(a–c)]. When the $CaCO_3$ dosage is more than 2 wt %, the penetrability and the number of pores decrease with the further addition of $CaCO_3$ [shown as Figure 9(d–f)].

In this work, the ultimate morphology and structure of a membrane are determined by the two factors: L-L phase separation and polymer crystallization. The crystallization process of a semicrystalline polymer involves nucleation and crystal growth. With no $CaCO_3$ addition, the crystal nuclei formed as homogeneous nucleation. The T_C of M-0 is the lowest (shown as Figure 7) because of the high activation energy for the formation of crystal nuclei.[42] The quantity of crystal nuclei increased gradually during crystallization. PVDF molecular chains were cross-linked around the nuclei. The crystal nuclei formed and grew in nonuniform size.

When $CaCO_3$ nanoparticles were introduced to the casting solution, the crystal nuclei formed as heterogeneous nucleation. $CaCO_3$ nanoparticles acted as the crystal nuclei in the crystallization process of PVDF molecules. When the $CaCO_3$ dosage was no more than 2 wt %, with the increase of $CaCO_3$ dosage, there were more nuclei available in the system, and the system remained uniform and stable. The addition of $CaCO_3$ nanoparticles promoted the crystallization process of PVDF molecules. The T_C increases in the phase diagram as a consequence. The dimensions of crystals decreased with the nuclei increasing as the polymer concentration was constant, which enhanced the connectivity of the spaces that the diluent occupied in the crystallization process. Thus, the penetrability and the number of pores increased correspondingly. When the $CaCO_3$ dosage was more than 2 wt %, aggregation happened in the system due to the redundant $CaCO_3$ nanoparticles in the polymer matrix, which meant that the dimensions of the crystal nuclei were not uniform. Thus, the crystallization process of PVDF molecules became inhomogeneous. On the other hand, some of the space that should have belonged to the diluents was occupied by the aggregated nanoparticles. Therefore, the penetrability and the number of pores decreased [shown as Figure 9(d–f)].

Hydrophobicity Analysis

The surface hydrophobicity has an influence on the flux and antifouling ability of the membrane. The contact angle between water and the outer surface of a hollow fiber membrane was measured in order to determine the membrane hydrophobicity. As shown in Table IV, the contact angle increases with the $CaCO_3$ nanoparticle addition. The surface roughness affects the value of the contact angle directly. AFM analysis was used to evaluate the surface roughness of membranes. Figure 10 presents three-dimensional AFM images of the membrane outer surface. It can be seen that the membrane outer surfaces become rougher with the increase of $CaCO_3$ dosage. The average roughness values are also listed in Table IV. The average roughness of the PVDF/$CaCO_3$ hybrid membranes are higher than the pure membrane. This indicates that the addition of $CaCO_3$ nanoparticles is an effective method to improve membrane hydrophobicity.

Table IV. Water Contact Angles and Average Roughness Values

Sample	Contact angle (°)	Average roughness (nm)
M-0	86.65 ± 2.01	127.46
M-1	91.44 ± 1.65	149.66
M-2	94.13 ± 1.83	292.53
M-3	95.59 ± 1.69	305.92
M-5	98.74 ± 1.93	349.70
M-8	103.21 ± 2.04	529.41

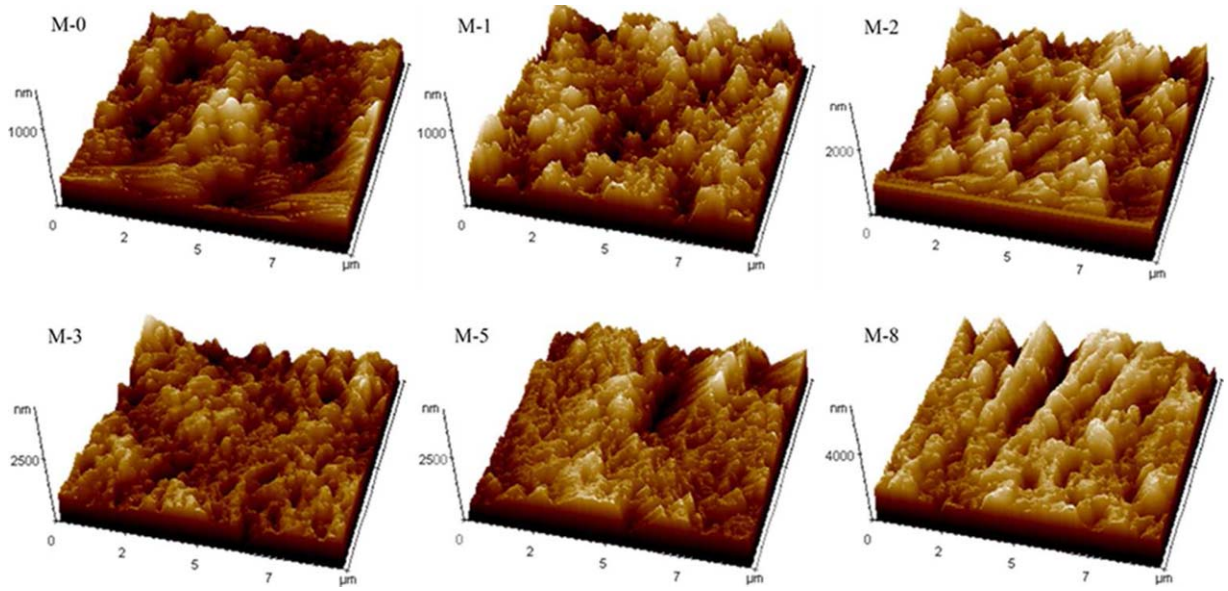

Figure 10. AFM images of the outer surfaces of membranes with different $CaCO_3$ dosages. [Color figure can be viewed in the online issue, which is available at wileyonlinelibrary.com.]

Porosity, Mean Pore Size, and Pore Size Distribution of Hollow Fiber Membranes

The theoretical and actual porosity of membranes are listed in Table V. It is obvious that the actual porosity of each membrane is usually lower than the theoretical porosity. This is mainly attributed to the evaporation of diluent in the membrane fabrication process. A portion of the diluent, which evaporated at the outer surface of the membrane, did not remain in the membrane and take up the space among the polymer molecules. When the S-L phase separation occurred, there was more space for polymer molecules to crystallize and grow, which led to the smaller porosity than the theoretical value.

The mean pore size and pore size distribution of membranes with $CaCO_3$ dosage varied from 0 wt % to 8 wt % are shown in Figure 11. As discussed, when the $CaCO_3$ dosage was no more than 2 wt %, the nanoparticles provided homogeneous crystal nuclei in the system. The crystallization process of the polymer tended to be gradually uniform. Therefore, the pore size distribution becomes narrower with the increase of $CaCO_3$ dosage. And the mean pore size is getting bigger, which demonstrates that the moderate amount of $CaCO_3$ improved the connectivity among the pores. The highest porosity is obtained when the addition of $CaCO_3$ nanoparticles is 2 wt %. When $CaCO_3$ dosage exceeded 2 wt %, the growth space of pores was compressed by the aggregated $CaCO_3$ nanoparticles, and the polymer crystallization became irregular. On the other hand, the aggregation of $CaCO_3$ nanoparticles weakened the connectivity of the pores and increased the number of closed pores simultaneously. Therefore, the pore size distribution moves to the low-dimension region, and the porosity declines accordingly.

Table V. Comparison between Theoretical and Actual Porosities of Membranes with Different $CaCO_3$ Dosages

Sample	Theoretical porosity (%)	Actual porosity (%)
M-0	82.45	66.76 ± 1.24
M-1	82.38	68.52 ± 1.33
M-2	82.29	69.71 ± 1.06
M-3	82.19	69.06 ± 1.18
M-5	82.05	68.24 ± 1.15
M-8	81.72	67.33 ± 1.27

Mechanical Properties of Hollow Fiber Membranes

Tensile strength is an important factor that reflects the mechanical properties of the PVDF hollow fiber membranes. The effect of $CaCO_3$ dosage on the tensile strength of the membranes is illuminated in Figure 12. With the increase of $CaCO_3$ dosage, the tendency is for tensile strength to increase at first and then decrease. This phenomenon may be attributed to the appropriate dosage of $CaCO_3$, which is beneficial to forming a stable and homogeneous membrane structure. The cellular structure distributed the external force on the membrane uniformly, which made the membrane exhibit a higher tensile strength. However, an excessive amount of $CaCO_3$ caused the aggregation of nanoparticles. The redundant nanoparticles dispersed inhomogeneously in the polymer matrix, which affected the membrane structure and formed many stress-convergence points in the membrane under the external force. Therefore the mechanical stability of the membrane was weakened accordingly. A similar result was reported in the literature.[23] The degree of crystallinity affects the membrane mechanical properties as well. The interaction among the molecules of crystalline polymer is stronger than for the amorphous polymer, so the membrane with a higher degree of crystallinity exhibits a higher tensile strength.

Dead End Pure Water Flux of Hollow Fiber Membranes

Pure water flux is one of the important indexes in evaluating the permeability of a membrane. The effect of $CaCO_3$ dosage

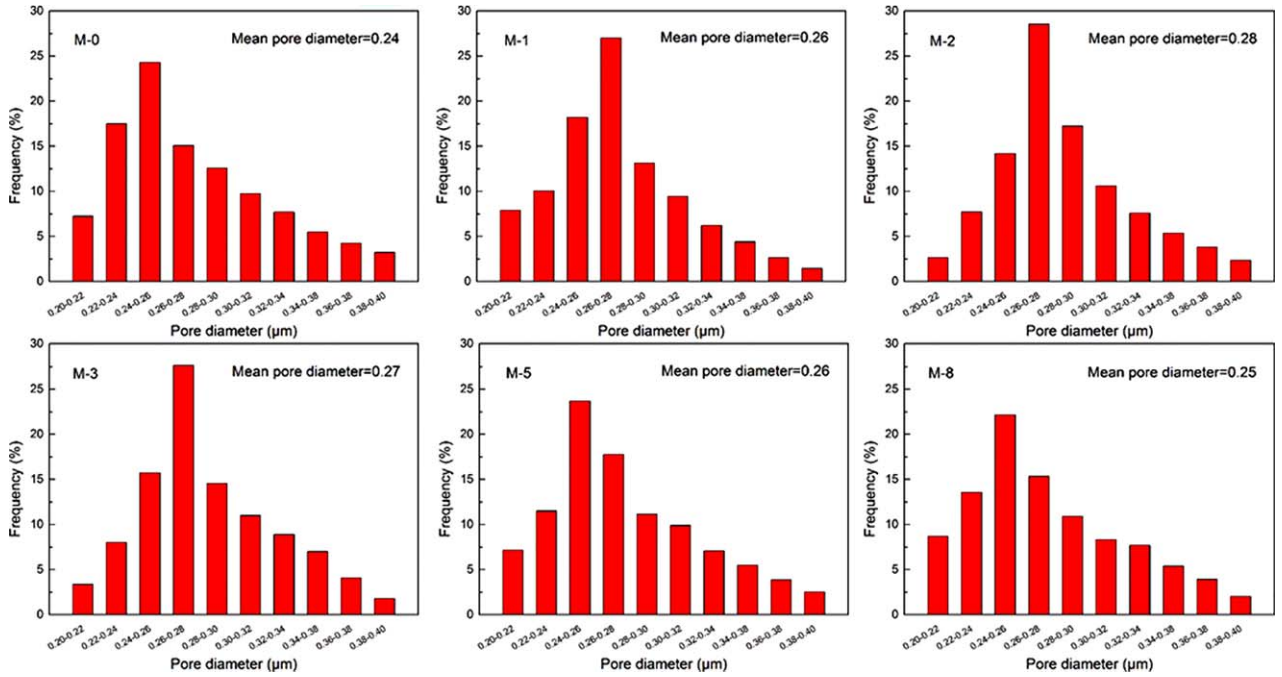

Figure 11. Mean pore size and pore size distribution of membranes with different $CaCO_3$ dosages. [Color figure can be viewed in the online issue, which is available at wileyonlinelibrary.com.]

on the water flux of hollow fiber membranes is elucidated in Figure 13. It shows that all of the PVDF/$CaCO_3$ hybrid fibers have higher water flux than the pure PVDF membrane. The water flux first increases and then decreases as $CaCO_3$ nanoparticles increase in the hybrid membranes. Since the porosity and pore size are the most important factors affecting the water flux, the tendency for water flux is similar to the porosity and pore size, as investigated in the previous section. As the $CaCO_3$ dosage increases from 0 wt % to 2 wt %, the pore size distribution becomes narrow gradually and the mean pore size and porosity increase, which are beneficial to water permeation. Thus, the pure water flux increases correspondingly. When the $CaCO_3$ dosage continues to increase, the growth space of pores is compressed because of the aggregation of redundant nanoparticles. Therefore, the pore size distribution moves to the low-dimension region, and the number of pores and porosity decrease respectively. The irregular structure becomes the inevitable obstacle when water went through the membranes. Therefore, the water flux shows a tendency to decrease.

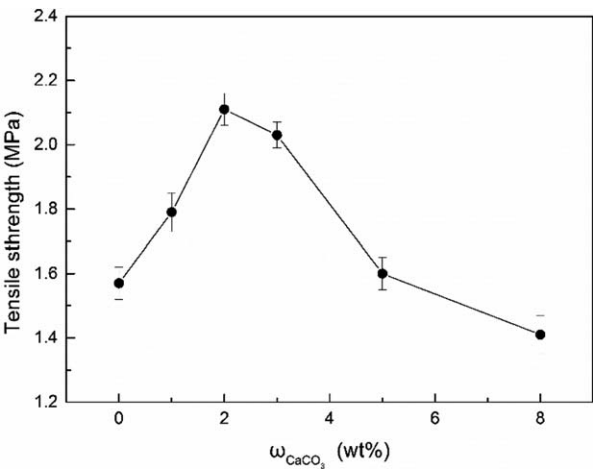

Figure 12. Tensile strength of membranes with different $CaCO_3$ dosages.

DCMD Flux of Hollow Fiber Membranes

The membrane is the basis and core part of the membrane distillation process. The DCMD test is the most simple and effective method to evaluate the membrane performance for applications. In the DCMD process, the hot feed temperature ranged from 50 °C to 90 °C. The vapor pressure increased as the temperature rose, so the driving force was improved accordingly. The electrical conductivity of the cold side was maintained below 50 μS/cm, which meant that there was no leakage in the membranes and the

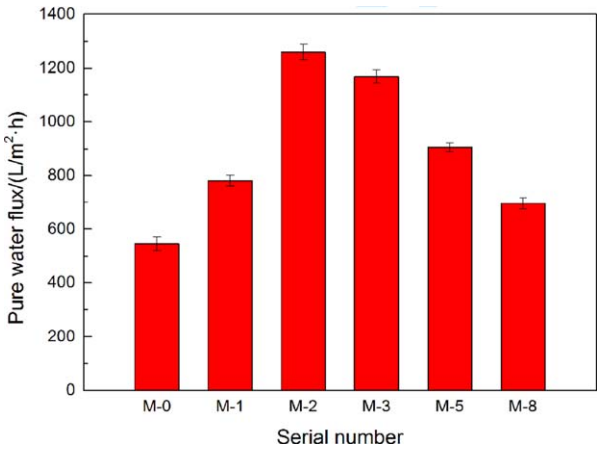

Figure 13. Water fluxes of membranes with different $CaCO_3$ dosages. [Color figure can be viewed in the online issue, which is available at wileyonlinelibrary.com.]

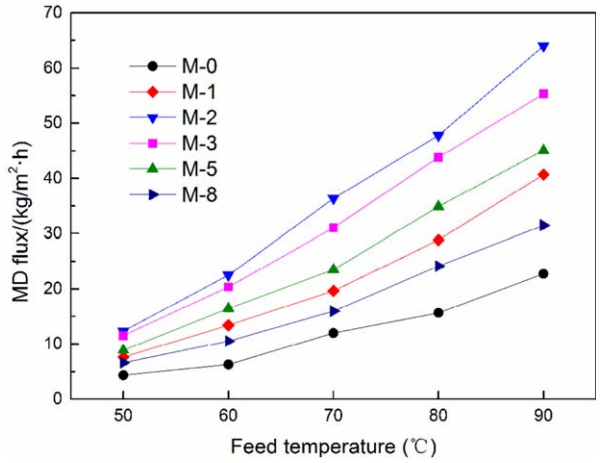

Figure 14. DCMD fluxes of membranes with different $CaCO_3$ dosages. [Color figure can be viewed in the online issue, which is available at wileyonlinelibrary.com.]

module. The result of the DCMD test is shown in Figure 14. In the test process, the vapor passed through the pores and went inside the membranes, while the water was resisted outside because of the hydrophobicity of PVDF. Both the DCMD and water flux are influenced by the porosity and pore size. Thereby, the DCMD flux presents the same tendency as the water flux. The detected conductivity of the cold distillate was stabilized at about 30–50 μS/cm, which indicated that the NaCl rejection of the membranes was above 99%. The conductivity and the rejection of M-2 in the DCMD are presented in Table VI to illustrate the separation performance of the membrane.

Table VII lists a performance comparison between the current work and the referenced works. It can be observed that the DCMD flux of M-2 achieves 63.98 kg/(m^2 h) at the feed temperature of 90 °C, which reaches the advanced level by comparing with the same kind of hollow fiber membranes reported in the literature.[6,15,32,43–47]

CONCLUSIONS

PVDF and PVDF/$CaCO_3$ hollow fiber membranes were prepared via an environmentally friendly TIPS method in this work. L-L phase separation played the leading role in the membrane fabrication process, which induced the membranes to have a cellular structure. The addition of $CaCO_3$ nanoparticles had an obvious influence on the properties of the membranes. The PVDF/$CaCO_3$ hybrid membranes exhibited better performance in crystallinity degree, hydrophobicity, porosity, and

Table VI. Conductivity and Rejection of M-2 in the DCMD

Temperature (°C)	Conductivity (μs/cm)	Rejection (%)
50	38.7	99.46
60	33.2	99.54
70	47.5	99.33
80	40.1	99.44
90	43.9	99.39

Table VII. Performance Comparison between the Current Work and the References

			Feed solution			Permeate solution		
Membrane	Permeate flux (kg/(m^2 h))	Rejection (%)	NaCl concentration (wt %)	Temperature (°C)	Flow rate (m/s)	Temperature (°C)	Flow rate (m/s)	Reference
PVDF hollow fiber membrane	51.5	99.99	3.5	90	0.04	20.0	0.04	15
PVDF hollow fiber membrane	41.5	99.99	3.5	79.3	1.60	17.5	0.80	43
PVDF hollow fiber membrane	40.5	99.99	3.5	81.8	0.50	20	0.15	44
PVDF dual-layer hollow fiber membrane	55.2	99.8	3.5	90.3	1.60	16.5	0.80	45
PVDF dual-layer hollow fiber membrane	66.9	99.8	3.5	78.2	1.8	16.6	0.72	46
PVDF/$CaCO_3$ hollow fiber membrane	46.3	99.99	3.5	80.5	0.50	20.0	0.15	32
PVDF/clay hollow fiber membrane	79.2	100	3.5	81.3	1.8	17.5	1.2	6
PVDF/PTFE dual-layer composite hollow fiber	52.5	100	3.5	80	1.90	17.5	0.90	47
This work	63.98	99.39	3.5	90	1.00	25.0	0.80	

permeability in comparison with the pure PVDF membrane. The DCMD performance of the PVDF/$CaCO_3$ hybrid membranes reached the internationally advanced level. The optimum $CaCO_3$ addition to the membrane was 2 wt %. The maximum DCMD flux achieved was 63.98 kg/(m^2 h) with NaCl rejection of 99.39% at the feed temperature of 90 °C, which was almost three times the flux of the membrane without $CaCO_3$ addition.

ACKNOWLEDGMENTS

This work was supported by the Science and Technology Pillar Program of Sichuan Province (No. 2014GZ0077). Meanwhile the authors gratefully acknowledged the Science and Technology Project of Tianjin China (No. 12ZCZDSF02200).

REFERENCES

1. García-Payo, M. C.; Rivier, C. A.; Marison, I. W.; von Stockar, U. *J. Membr. Sci.* **2002**, *198*, 197.
2. Rivier, C. A.; García-Payo, M. C.; Marison, I. W.; von Stockar, U. *J. Membr. Sci.* **2002**, *201*, 1.
3. Tijing, L. D.; Woo, Y. C.; Choi, J. S.; Lee, S.; Kim, S. H.; Shon, H. K. *J. Membr. Sci.* **2015**, *475*, 215.
4. Shirazi, M. M. A.; Kargari, A.; Shirazi, M. J. A. *Desalin. Water Treat.* **2012**, *49*, 368.
5. Abdallah, S. B.; Frikha, N.; Gabsi, S. *Desalin. Water Treat.* **2014**, *52*, 2362.
6. Wang, K. Y.; Foo, S. W.; Chung, T. S. *Ind. Eng. Chem. Res.* **2009**, *48*, 4474.
7. Wu, L.; Sun, J.; Wang, Q. *J. Membr. Sci.* **2006**, *285*, 290.
8. Devi, S.; Ray, P.; Singh, K.; Singh, P. S. *Desalination* **2014**, *346*, 9.
9. Liu, F.; Hashim, N. A.; Liu, Y.; Abed, M. R. M.; Li, K. *J. Membr. Sci.* **2011**, *375*, 1.
10. Du, C. H.; Xu, Y. Y.; Zhu, B. K. *J. Appl. Polym. Sci.* **2007**, *106*, 1793.
11. Kim, J.; Kim, S. S.; Park, M.; Jang, M. *J. Membr. Sci.* **2008**, *318*, 201.
12. Mulder, M. Basic Principles of Membrane Technology; Kluwer Academic: Dordrecht, **1996**.
13. Hashim, N. A.; Liu, Y.; Li, K. *Ind. Eng. Chem. Res.* **2011**, *50*, 3035.
14. Kang, G. D.; Cao, Y. M. *J. Membr. Sci.* **2014**, *463*, 145.
15. Song, Z.; Xing, M.; Zhang, J.; Li, B.; Wang, S. *Sep. Purif. Technol.* **2012**, *90*, 221.
16. Roh, I. J.; Ramaswamy, S.; Krantz, W. B.; Greenberg, A. R. *J. Membr. Sci.* **2010**, *362*, 211.
17. Wang, Z.; Sun, L.; Wang, Q.; Li, B.; Wang, S. *Eur. Polym. J.* **2014**, *60*, 262.
18. Rajabzadeh, S.; Maruyama, T.; Sotani, T.; Matsuyama, H. *Sep. Purif. Technol.* **2008**, *63*, 415.
19. Cao, X.; Ma, J.; Shi, X.; Ren, Z. *Appl. Surf. Sci.* **2006**, *253*, 2003.
20. Yang, Y.; Zhang, H.; Wang, P.; Zheng, Q.; Li, J. *J. Membr. Sci.* **2007**, *288*, 231.
21. Shi, F.; Ma, Y.; Ma, J.; Wang, P.; Sun, W. *J. Membr. Sci.* **2013**, *427*, 259.
22. Yu, L. Y.; Xu, Z. L.; Shen, H. M.; Yang, H. *J. Membr. Sci.* **2009**, *337*, 257.
23. Liang, S.; Xiao, K.; Mo, Y.; Huang, X. *J. Membr. Sci.* **2012**, *394–395*, 184.
24. Liu, F.; Abed, M. R. M.; Li, K. *J. Membr. Sci.* **2011**, *366*, 97.
25. Yan, L.; Li, Y. S.; Xiang, C. B.; Xianda, S. *J. Membr. Sci.* **2006**, *276*, 162.
26. Bottino, A.; Capannelli, G.; Comite, A. *Desalination* **2002**, *146*, 35.
27. Ngang, H. P.; Ooi, B. S.; Ahmad, A. L.; Lai, S. O. *Chem. Eng. J.* **2012**, *197*, 359.
28. Cui, A.; Liu, Z.; Xiao, C.; Zhang, Y. *J. Membr. Sci.* **2010**, *360*, 259.
29. Hou, D.; Wang, J.; Sun, X.; Luan, Z.; Zhao, C.; Ren, X. *J. Hazard. Mater.* **2010**, *177*, 613.
30. Tran, H. V.; Tran, L. D.; Vu, H. D.; Thai, H. *Colloids Surf., A* **2010**, *366*, 95.
31. Li, X.; Lu, X. *J. Appl. Polym. Sci.* **2006**, *101*, 2944.
32. Hou, D.; Wang, J.; Sun, X.; Ji, Z.; Luan, Z. *J. Membr. Sci.* **2012**, *405–406*, 185.
33. Tang, Y.; Lin, Y.; Ma, W.; Tian, Y.; Yang, J.; Wang, X. *J. Appl. Polym. Sci.* **2010**, *118*, 3518.
34. Marega, C.; Marigo, A. *Eur. Polym. J.* **2003**, *39*, 1713.
35. Li, X.; Wang, Y.; Lu, X.; Xiao, C. *J. Membr. Sci.* **2008**, *320*, 477.
36. Ji, G.; Zhu, L.; Zhu, B.; Zhang, C.; Xu, Y. *J. Membr. Sci.* **2008**, *319*, 264.
37. de C. Campos, J. S.; Ribeiro, A. A.; Cardoso, C. X. *Mater. Sci. Eng., B* **2007**, *136*, 123.
38. Lloyd, D. R.; Kinzer, K. E.; Tseng, H. S. *J. Membr. Sci.* **1990**, *52*, 239.
39. Lloyd, D. R.; Kim, S. S.; Kinzer, K. E. *J. Membr. Sci.* **1991**, *64*, 1.
40. van de Witte, P.; Dijkstra, P. J.; van den Berg, J. W. A.; Feijen, J. *J. Membr. Sci.* **1996**, *117*, 1.
41. Matsuyama, H.; Takida, Y.; Maki, T.; Teramoto, M. *Polymer* **2002**, *43*, 5243.
42. Shi, F.; Ma, Y.; Ma, J.; Wang, P.; Sun, W. *J. Membr. Sci.* **2012**, *389*, 522.
43. Yu Wang, K.; Chung, T. S.; Gryta, M. *Chem. Eng. Sci.* **2008**, *63*, 2587.
44. Hou, D.; Wang, J.; Qu, D.; Luan, Z.; Ren, X. *Sep. Purif. Technol.* **2009**, *69*, 78.
45. Bonyadi, S.; Chung, T. S. *J. Membr. Sci.* **2007**, *306*, 134.
46. Su, M.; Teoh, M. M.; Wang, K. Y.; Su, J.; Chung, T. S. *J. Membr. Sci.* **2010**, *364*, 278.
47. Teoh, M. M.; Chung, T. S.; Yeo, Y. S. *Chem. Eng. J.* **2011**, *171*, 684.